Lab on a Chip

ROYAL SOCIETY OF CHEMISTRY

PAPER

View Article Online
View Journal

Cite this: DOI: 10.1039/d5lc00417a

Morphing out-of-surface channels enable strain-based control over fluid flow in skin-mountable patches

Rana Altay,[a] Hudson Gasvoda,[a] Max Mailloux-Beauchemin,[b] Johanna Brown,[a] Kari Olson[a] and I. Emre Araci *[a]

Received 28th April 2025,
Accepted 13th August 2025

DOI: 10.1039/d5lc00417a

rsc.li/loc

The volume of natural materials increases under tension, thus conventionally biomechanical actuation of fluidic pumps relies on compression for pressure generation. Here, we report on out-of-surface microchannels (OSMiCs) that exhibit negative volumetric strain (*i.e.*, pressure generation) under skin-induced tensile strain. Monolithic polydimethylsiloxane (PDMS) patches were fabricated and characterized. The complex relations between the wrinkling and buckling of the OSMiC shell and the fluid flow patterns were investigated. OSMiCs were shown to snap-back (-through) between two stable states that lead to (ir) reversible fluid flow depending on their architecture. Unlike standard microchannels that only generate pressure symmetrically upon application and release of tensile strain, OSMiCs are shown to be tunable for providing an asymmetrical pressure owing to their shape-change property (*i.e.*, morphing). The maximum forward (backward) flow pressure of 10 (−14) kPa was measured upon 20% uniaxial strain application (release). The versatile fabrication technique allowed the integration of OSMiCs with different Q values, leading to a discrete strain-actuated flow control element. Numerical simulations were conducted and shown to support the experimentally observed wrinkling and buckling behavior. Finally, the operation of the power-free OSMiC skin patch for strain-based liquid administration on skin was demonstrated.

Introduction

Wearable microfluidic applications span from diagnostics[1–4] to therapeutic interventions (*e.g.*, wound healing,[5,6] drug delivery,[7] and personalized medicine[8–10]), and energy harvesting.[11,12] For these technologies, control over fluid flow is required to achieve various functions such as precise dosing, effective reagent mixing, and sample manipulation. Specifically, for drug delivery, a critical requirement is maintaining stable drug concentrations within a therapeutic window, which directly impacts treatment efficacy, reduces side effects, and prolongs the duration of action.[13–16] Automated, closed-loop feedback systems[17–21] that are attractive for achieving this, often require active pumping and rigid control elements that limit wearability. Utilizing human movement-induced skin-strain for microfluidic flow control can eliminate the need for electrical power and rigid components.[22] Since the strain that drives the fluid flow is initiated by the skin deformations, the user can generate the requisite force continuously through daily movements enabling a seamless and user-controlled manipulation of fluid flow without the need for an external power source.

Several benchtop studies have explored strain-induced microfluidic functions, such as valves,[23] and release mechanisms for trapped micro-entities.[24] On the other hand, human movement-based microfluidic flow generation remains largely limited to compression of hemispherical structures by finger actuation.[25–27] In an interesting application, Reeder *et al.* showed that extending a pull-tab in a microfluidic device can initiate pumping, but like finger pumps, this also requires a deliberate and specialized movement for activation[28] rather than relying on daily movements or exercises. In one example of skin stretching-based drug delivery, Di *et al.* utilized Poisson's ratio mismatch between hydrogels and elastomers for increasing the efficiency of molecular transport, however, there was no fluidic flow in this study.[29] While this was a promising advancement, challenges such as drug depletion and lengthy recharging times remained. Integrating microfluidic systems could offer a potential solution by enabling precise control over drug diffusion and release, thereby improving consistency and efficiency.

Fluidic control mechanisms using morphing behavior have gained interest due to their promise to reduce the complexity, mass, and actuation power.[30] Morphing

---

[a] *Department of Bioengineering, Santa Clara University, CA 95053, USA. E-mail: raltay@scu.edu, iaraci@scu.edu*
[b] *Mechanical Engineering Department, Santa Clara University, CA 95053, USA*

structures change shape in response to an input load in a fast and nonlinear manner.[31–34] For example, their implementation as valves was shown to improve fluid control capabilities for systems that utilize strain as the actuation mechanism.[35,36] Additionally, the interaction between the fluid flow dynamics and morphing is shown to play a role in fluidic control. Gomez *et al.*[31] utilized a macroscopic elastic arch to regulate fluid flow using the snapping behavior of an arch, which transitions between two distinct states depending on the fluid flux. Initially, the arch partially constricts the channel, reducing the flow. At a threshold flow rate, the arch rapidly snaps through, removing the constriction and drastically decreasing the hydraulic resistance. The required snapping threshold pressure increases with the bending stiffness of the membrane and the arch height.

Snap-through or -back represents a buckling instability that provides the ability to transition suddenly between two stable states.[30,32,37,38] This phenomenon appears in various natural systems, including plant mechanisms and biological structures such as the Venus flytrap's leaf lobes utilize this instability to rapidly capture prey[39,40] and the hummingbird's lower jaw performs a snap to catch flying insects with remarkable speed.[41] This elastic instability has been widely used across diverse fields, ranging from fluid manipulation and soft robotics[42,43] to biomedical applications.[44] Theoretical analyses of snap-through phenomena have been conducted, resulting in the development of analytical models that predict critical conditions and system behavior.[32,33] These models have also been utilized to explore the effects of fluid–structure interactions on pumping and valve mechanisms driven by snap-through dynamics. Typically, the shallowness parameter, which signifies the ratio of stretching to bending energy, is used to characterize the morphing of dome-shaped structures.[45] For more simple curved beams, a simplified parameter is described by Chi *et al.* as Q, the aspect ratio, which is the ratio of arch height to membrane thickness.[38]

Despite significant advancements in snap-through instabilities for fluid manipulation, valve, and pump mechanisms, a critical gap remains in the development of fully passive, self-regulated microfluidic systems for wearable applications. Current approaches often require external power sources or complex control systems to drive liquid flow and trigger snap-through transitions, limiting their practical implementation in wearables. In this study, we address this fundamental limitation by integrating strain-driven microfluidics with morphing shells. First, we have created an out-of-surface microchannel (OSMiC) structure. Unlike conventional microfluidic channels where tensile strain creates negative pressure that draws liquid into the channel due to the volume expansion,[46–49] the OSMiC design features an arch shape shell (*i.e.*, a membrane that maintains its shape under externally applied loads[50]) that generates positive pressure when subjected to tensile strain, actively displacing the liquid toward the outlet. When strain is released, the vacuum inside the channel causes the morphing of the OSMiC shell. While the shell architecture is designed to show bi-stable behavior, the incomplete snap-through of structures with large Q results in a snap-back, akin to pseudo-stable structures.[30] Since this shape-change occurs without an external load, we call it self-morphing. We have characterized the self-morphing behavior of OSMiC structures under varying strain application/release conditions (0–20%) and systematically investigated the complex interplay between fluid dynamics and structural mechanics for various OSMiC geometrical parameters. We have identified architectures that can be utilized either for reversible or irreversible fluid flow during strain application/release cycle. We have also showed that a morphing microchannel can generate either symmetric or asymmetrical pressure patterns depending on its shell thickness and aspect ratios. Notably, under snap-through conditions, backward pressure is eliminated. These results are distinctly different from the conventional microfluidic channel behavior, which exhibit only symmetrical fluid pressure pattern (*i.e.*, identical forward and backward pressure) during application/release of strain.[51] Our findings reveal that increasing the Q increases the pressure generation capability with the exception of a single case, when wrinkling is reduced. This observation was also supported by the numerical simulations. Building on these findings, first, a fluid control method is introduced by the integration of two different OSMiC architectures to demonstrate the operation of a strain-induced valve. Second, we demonstrated that skin patches with OSMiCs can pump liquids while being powered by tensile strain induced by natural human movement, eliminating the need for external power sources (Fig. 1). Fig. 1 illustrates the concept of biomechanically activated wearable microfluidic system for drug delivery applications.

Materials and methods

Fabrication

A CAD model is designed for mold fabrication and transferred to a stereolithography 3D printer (Form 3+, FormLabs). After printing, molds undergo a three-step post-processing: washing with isopropyl alcohol (IPA) for 10 minutes, UV curing using the UVC-1000 device (Hoefer Inc.) at maximum energy for 5 minutes, and overnight baking at 80 °C. To fabricate PDMS (polydimethylsiloxane), (RTV 615, Momentive Inc.), OSMiC structures, we developed a modified thermal bonding method (mod-TB) that strategically utilizes PDMS shrinkage. While PDMS shrinkage is typically considered undesirable and can cause misalignment and leakage issues,[52,53] we repurposed this property as the fundamental mechanism for generating OSMiC structures. The shrinkage-driven OSMiC structures are created through the control of PDMS mixing ratios, spin speeds, baking time, and curing temperature. The process begins with spin-coating 10 : 1 PDMS onto a mold with microchannel patterns

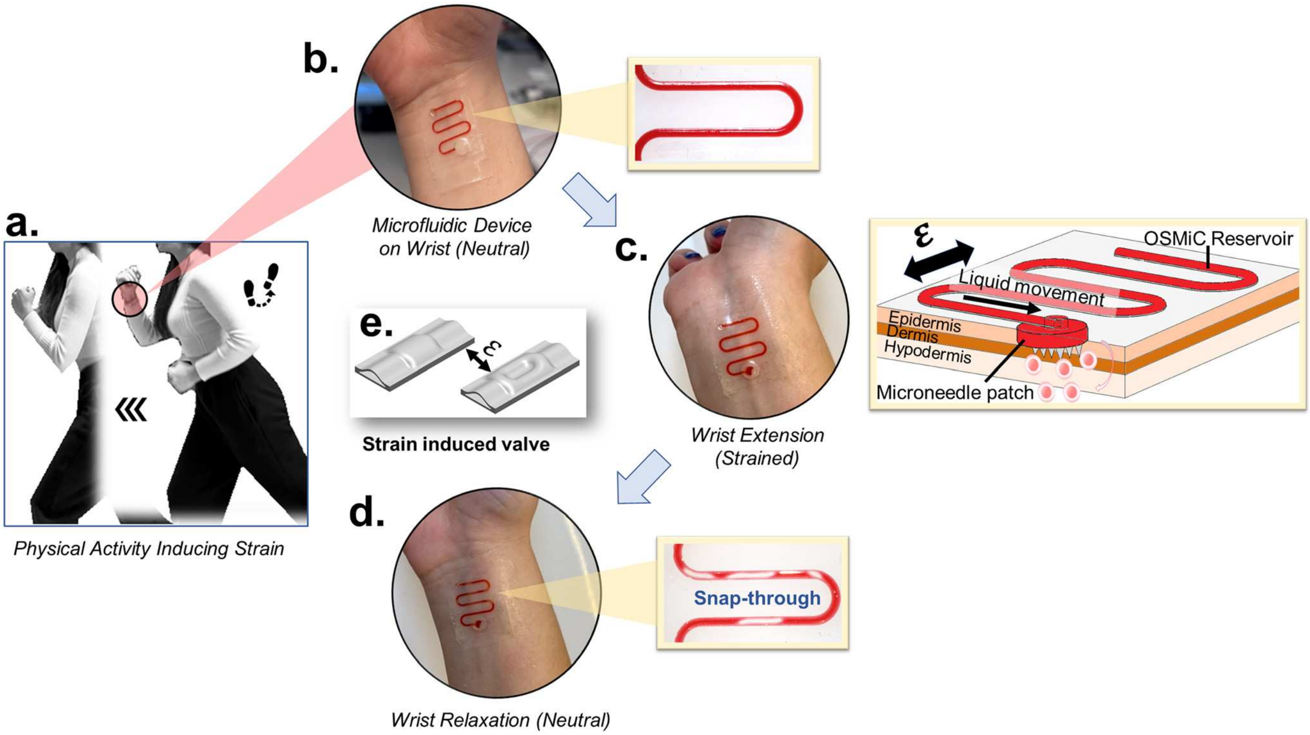

Fig. 1 Biomechanically activated wearable microfluidic system for drug delivery applications. The flow diagram reveals the operational principles of a skin-mounted microfluidic device that harnesses natural body movements for fluid transport. Photographs of the device mounted on the wrist display its conformality and seamless integration with the skin. The overall chip thickness is 300 μm. (a) Physical activities generate skin strain that activates the fluid delivery mechanism. (b–d) Sequential close-up photographs capture the serpentine microfluidic chip on the wrist in three distinct states: neutral position (b), extended configuration during wrist movement (c), and relaxed state following strain release (d). Adjacent yellow-bordered insets provide magnified views of the microchannels, illustrating membrane deformation patterns and liquid displacement dynamics during each phase. (e) The schematic at the center displays the integrated strain-induced valve mechanism that strategically combines different OSMiC channel geometries to control fluid flow through applied strain. This passive, motion-activated system enables automated drug delivery during physical activity without requiring external power sources.

with a width of 1 mm, adjusting spin speed according to the desired final thickness. After complete curing, this patterned PDMS layer is peeled off and placed onto a partially cured, sticky PDMS base layer (20 : 1 ratio) that has been spin-coated on a blank silicon wafer. The sticky PDMS base layer is achieved by curing the spin-coated layer in an 80 °C oven for 9 minutes resulting in a tacky surface. The combined structure is then baked at specific temperatures (45 °C, 120 °C, or 150 °C) to create different OSMiC heights. During this critical baking step, the shrinkage of the partially cured base layer induces controlled bulging of the channel ceiling, resulting in the formation of OSMiC reservoirs (Fig. S1a). Various thicknesses of the top layer and baking temperatures can be employed to achieve different OSMiC configurations (detailed in Fig. S1b and c). This approach is compatible with both 3D-printed molds and photolithography-made silicon wafers (cross-sections of photolithography-made structures are shown in Fig. S1d).

Experimental setup

To characterize the strain response of the microfluidic chips under benchtop conditions, we utilized a biaxial strain actuation system (Bi-SAS), as illustrated in Fig. S2a. The microfluidic chip was positioned in the center of the system, allowing for the application of tensile strain to the microchannel by adjusting the left and right components of the apparatus. To analyze the relationship between strain, morphing, and liquid displacement, it is crucial to use a hydrophobic working liquid. This ensures that liquid movement within the microchannel is solely driven by strain-induced flow, eliminating unintended displacement. Thus, the OSMiC reservoirs were filled with a working fluid composed of 50% DI water, 50% vegetable glycerin (365 Whole Foods Market, USA), and red food dye (Lorann, Michigan) for visualization purposes. For the analysis of the displaced volumes, liquid displacement length was determined using ImageJ software (National Institutes of Health). To obtain the cross-sectional images of OSMiCs, the microfluidic chip was manually cut perpendicular to the channel direction using a razor blade after experiments, exposing the internal geometry. The exposed section was then imaged using a Leica S9i stereo microscope at maximum optical zoom under ambient conditions which allowed to directly visualize key structural features such as shell thickness and OSMiC height.

To calculate the maximum pressure using experimental method, the air reservoir with varying volumes were created. To do this, the channel was punched at the outlet using different puncher sizes. After punching, the reservoir was sealed on both the top and bottom with a thin layer of PDMS, effectively creating a confined air pocket.

To investigate the relationship between strain and vacuum effects on shell morphing, controlled experiments were conducted using a microfluidic computerized pressure control system OB1 MK3+ (Elveflow, Elvesys). The OSMiC reservoir was first filled with working fluid and the outlet was sealed to maintain system integrity. A microfluidic tubing was then inserted into the inlet and connected to the Elveflow OB1 MK3+ pressure controller. For experiments requiring simultaneous strain application, the Bi-SAS was integrated with the setup to provide tensile strain while monitoring pressure-induced deformation. For sealing the outlets, a hard-type UV-curable resin (JDiction) was applied and subsequently cured under ultraviolet light.

In preparation for human subject testing, the fabricated microfluidic chips were integrated with a patch (Mighty Patch, Hero) at the outlet section of the microchannel. A specialized skin adhesive (Skin Tite, Smooth-On) was applied to the subject's skin in a 1 : 1 ratio. Following application, a 15 minute waiting period was observed before conducting tests to ensure a strong and secure bond between the skin and the microfluidic chip, thereby guaranteeing reliable and stable testing conditions.

2D digital image correlation (DIC) was used to calculate the skin strain field and quantify strain during wrist extensions. Detailed information on the DIC analysis can be found in the referenced study.[46]

Numerical modeling

We used COMSOL Multiphysics software for device modeling. Specifically, the "Shell physics" was utilized for characterizing the wrinkling and buckling behavior. A 0.8 cm long, 1 mm wide parabolic arch, with a 50 μm thick shell representing the OSMiC structure was placed in the center of a 500 μm thick rectangular shell with 1 cm by 2 cm dimensions. The strain was applied to the rectangular shell using prescribed displacement. The vacuum was applied only on the OSMiC shell using the face load. Both linear buckling analysis and stationary simulations of Von Mises stress were completed. Due to the similarity of the results, only stationary simulation results are shown here. The mechanical load was changed with an auxiliary sweep and the load value where the wrinkles were observed visually was used as the wrinkle strain threshold. The geometric nonlinearities were included but the material was linear. The internal PDMS properties of COMSOL were used as mechanical parameters of both shells. An isotropic spring foundation was assigned to both shells. The mesh for the OSMiC shell was manually mapped with 50 × 20 nodes to minimize computational errors.

Results

Systematic investigation of the key OSMiC parameters—including height (h), shell thickness (t_{m}), and channel base height (h_{base}) as shown in Fig. 2—has been conducted to analyze the morphing characteristics and associated fluid control mechanisms. Fig. 2a presents cross-sectional images comparing OSMiC architectures with varying Q values for a consistent shell thickness of 50 μm, alongside a microchannel without curvature. We analyzed three distinct curvature categories based on Q values and their fluidic responses: low-curvature ($Q = 2.1 \pm 0.6$), mid-curvature ($Q = 3.2 \pm 0.6$), and high-curvature ($Q = 4.3 \pm 0.4$). Fig. 2b presents the contact angle measurement (90°) on PDMS material. Nearly zero capillary pressure was achieved to eliminate the fluid movement except when induced by skin strain. Fig. 2c shows the diagram of the microfluidic channel layout, where the sealed inlet, outlet, liquid interface position, and strain (ε) direction are labeled.

In Fig. 2d, cartoon sketches of channel cross-sections with different Q-values during strain application/release are represented. Inset images (red dashed boxes) provide top-down experimental images that capture the corresponding wrinkling/buckling patterns. When strain is applied, both channel types experience curvature reduction, with low-curvature channels (rounded to $Q = 2$, for brevity) flattening almost completely while high-curvature channels ($Q = 4$) retain partial curvature. Interestingly, there is a visible wrinkle formation in high-curvature channels, whereas low-curvature channels do not show wrinkle formation. Wrinkle formation due to the compressive stresses in an orthogonal direction to the applied stretching in thin rectangular,[54,55] spherical,[56] and cylindrical[57] membranes have been demonstrated and analyzed extensively. The residual curvature of the high-curvature (up to $Q = 4$) OSMiC under strain is favorable for the formation of wrinkles.

The applied tensile strain and the resulting negative volumetric strain creates internal pressure. Upon the release of the tensile strain, the vacuum due to the sudden volume expansion, applies a uniform load to the shell and triggers buckling, which is intensified, as shown later, with the presence of wrinkles. This buckling results in a horizontally elongated pattern along the length of the microchannel in low-curvature channels. For high-curvature channels, the buckling occurs as periodic patterns, reflecting the distinct deformation behaviors influenced by Q. Chi *et al.* demonstrated that[38] there is a critical threshold, $Q_{\mathrm{cr}} = 2.31$ where the morphing 1D structures become bistable, characterized by two distinct stable equilibrium states. In reasonable agreement with this study, we observed snap-through behavior to the second stable state at $Q = 2$. The discrepancy could be explained by the differences in the geometry (*i.e.*, 1D *vs.* 3D structure). However, for $Q = 4$, the structure that should show a bistable character initially buckles but then rapidly snap-back to the original configuration. We attribute this behavior to the limited space

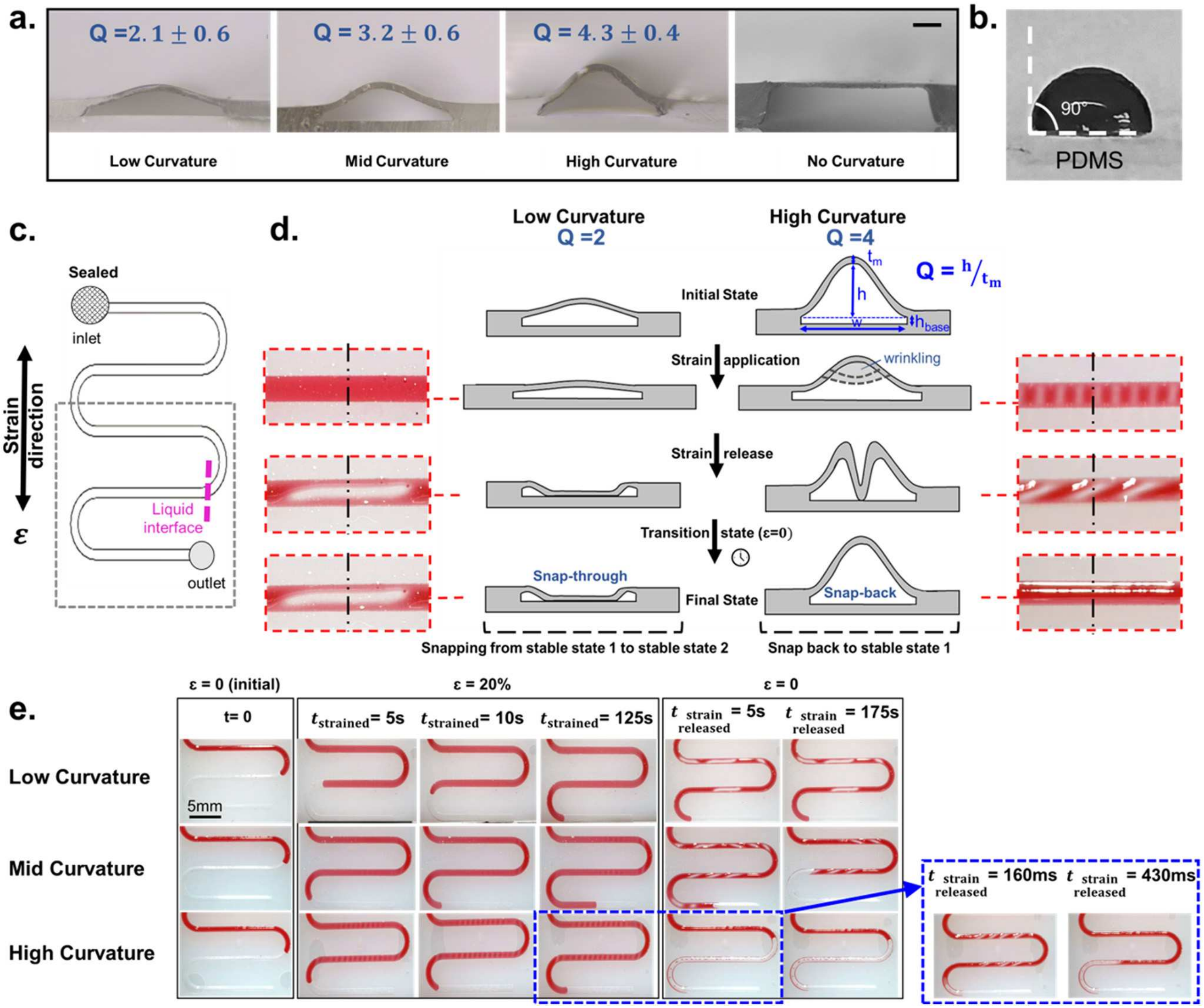

Fig. 2 Strain-responsive morphing characteristics of OSMiC structures and the resulting impact on fluid dynamics. (a) Cross-sectional images showing different curvature states quantified by parameter Q: low-curvature (Q = 2.1 ± 0.6), mid-curvature (Q = 3.2 ± 0.6), high-curvature (Q = 4.3 ± 0.4), and no curvature. Scale bar: 200 μm. (b) Contact angle measurement (90°) of a working fluid composed of 50% deionized (DI) water, 50% vegetable glycerin, and red food dye on PDMS material. (c) Diagram of the microfluidic channel depicting the microfluidic channel layout. (d) Cross-sectional images of the mechanical response of microfluidic channels. Inset images (red dashed boxes) provide top-down experimental images. (e) Time-lapse images of liquid movement within the microfluidic channel region (highlighted by dashed lines in diagram g) across different curvature conditions during strain application (ε = 20%) at t = 0, 5 s, 10s, and 125 s, followed by strain release (ε = 0). Rapid snap-back mechanics for high curvature channels at additional time points of 160 ms and 430 ms after strain release are shown in blue dashed boxes. Scale bar: 5 mm.

of the base channel not allowing a complete snap-through as illustrated in Fig. 2d.

Fig. 2e shows the photos of the liquid movement during strain application (ε = 20%) and release for low, mid, and high curvatures. The structure without any curvature does not show any measurable liquid movement under strain as shown in Fig. S3. In the first column (t = 0), the initial position of the liquid interface is shown. When tensile strain is applied, positive pressure within the OSMiC reservoir is generated, pushing the liquid forward. The second and third columns (t_{strained} = 5 s and t_{strained} = 10 s) demonstrate the progressive movement of the liquid toward the outlet. By approximately 40 seconds, liquid displacement stabilizes, and no further movement is observed. Upon strain release, in low-curvature channels (top), the shell undergoes snap-through behavior, remaining permanently buckled after strain release with the fluid remaining in its pushed position without being pulled back. Mid-curvature channels (middle) show partial shell recovery, with the shell slowly opening in some regions and driving liquid back toward its initial position, though buckling persists partially even after 175 seconds post-strain release ($t_{\text{strain-released}}$ = 175 s). In high curvature channels (bottom), the vacuum generated within the microchannel creates a pressure differential that actively pulls the liquid back toward its initial position. As the liquid moves, it exerts force on the buckled shell, causing it to pop back into its original configuration. This rapid snap-back behavior results in significantly faster fluid dynamics, as captured at additional time points of 160 ms and 430 ms after strain release (blue dashed boxes), with the shell quickly returning to its original state. SI videos illustrating liquid displacement behavior are provided for low-, mid-, and high-curvature channels in Videos S1–S3, respectively.

Quantitative measurements were conducted using three independently fabricated chips for each Q value, and the results are presented in Fig. 3, with averages and standard deviations plotted. The measurements confirm the

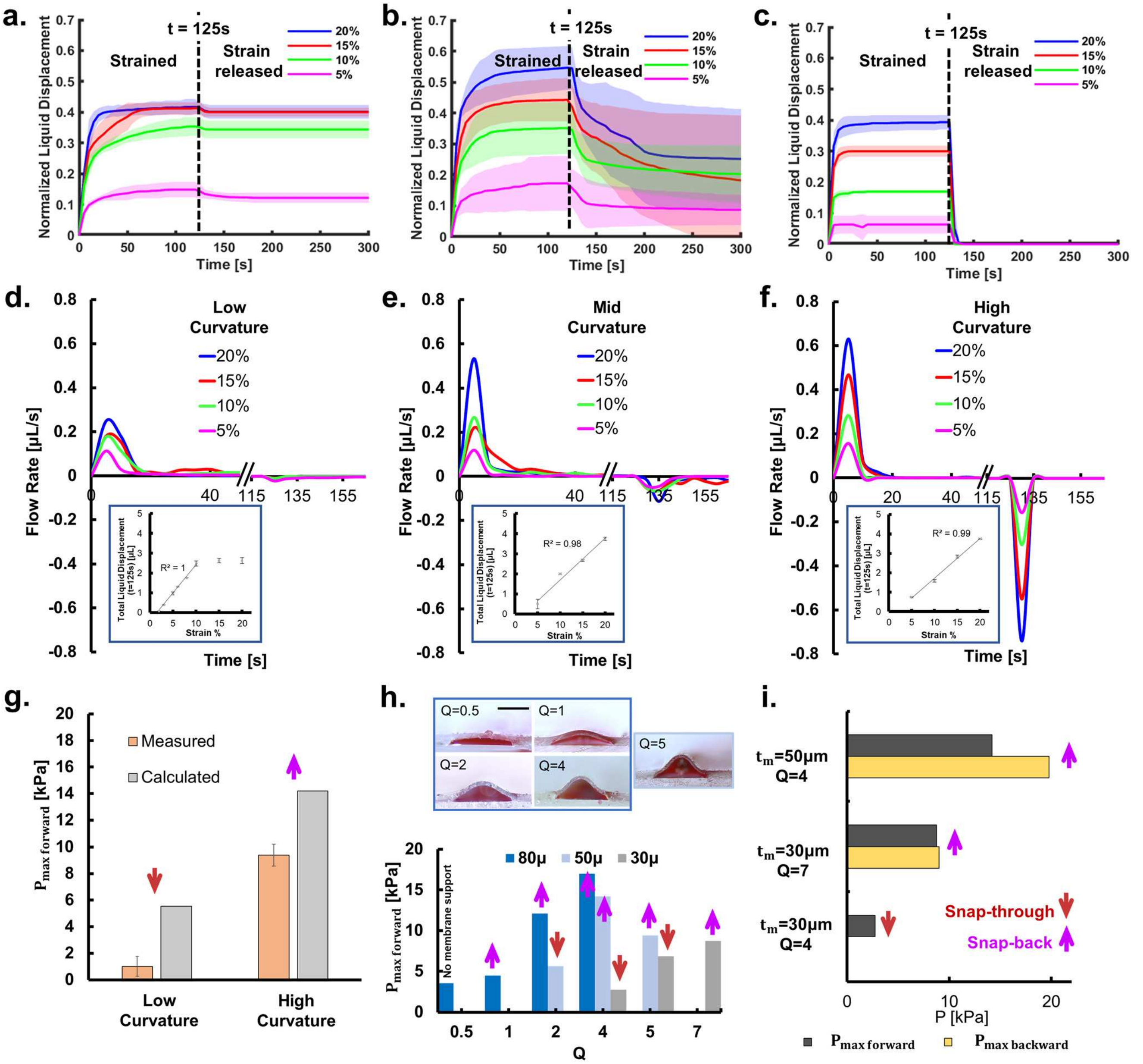

Fig. 3 The fluid dynamics and pressure characterization of strain-responsive microfluidic channels with varying curvature geometries. (a–c) Normalized liquid displacement over time at various strain levels (5%, 10%, 15%, and 20%) for (a) low-curvature, (b) mid-curvature, and (c) high-curvature channels. The vertical dashed line at t = 125 s indicates the strain release point, distinguishing between strained and strain-released states. (d–f) Flow rate measurements over time at different strain levels for (d) low-curvature, (e) mid-curvature, and (f) high-curvature channels. Insets show the linear relationship between total liquid displacement and applied strain percentage. Error bars indicate the standard deviation from three repeated measurements. (g) Comparison between measured (orange) and calculated (gray) maximum forward pressure ($P_{\text{max-forward}}$) for low- and high-curvature channels at t_m = 50. Measured data represents the maximum pressure obtained at $V_{\text{reservoir}}$ = 0.35 μL. Standard deviation is obtained from independently fabricated chips. (h) Cross-section images of channels with varying curvature parameters (Q = 0.5, 1, 2, 4 with 80 μm shell thickness and Q = 5 with 50 μm shell thickness) (top) and corresponding maximum forward pressure ($P_{\text{max-forward}}$) calculations for different shell thicknesses (30 μ, 50 μ, and 80 μ) across Q values (bottom). Scale bar: 500 μm. (i) Plot demonstrating the maximum forward and backward pressures for different shell thicknesses (t_m) and aspect ratios (Q).

characteristic visual observations described in Fig. 2. The time responses of the normalized liquid displacement in low-, mid-, and high-curvature channels, capturing the transition from the initial state to the strained state and following strain release, are represented at various strain levels (5%, 10%, 15%, and 20%) in Fig. 3a–c, respectively. The vertical dashed line at t = 125 s indicates the strain release point. The magnitude of liquid displacement during strain application increases with higher strain levels in mid- and high-curvature channels. In low-curvature channels, however, the increase in liquid displacement is primarily observed at lower strain levels (0–10%), while higher strains (15% and 20%) result in similar amounts of liquid displacement. Notably, the response times differ, as 20% strain induces a more rapid liquid push compared to 15% strain. The multi-cycle behavior of channels under repeated strain application and release is presented in Fig. S4.

The flow rates were calculated from the derivative of liquid displacement at different strain levels for low-, mid-, and high-curvature channels and are shown in Fig. 3d–f. Each condition shows an initial positive flow rate during strain application (0–40 s), followed by flow stabilization. After strain release (at t = 125 s), high-curvature channels (Fig. 3f) demonstrate significant negative flow rates, indicating rapid fluid retraction, while low-curvature channels (Fig. 3d) show negligible backward flow. The insets display experimental results from three repetitions of the chips, highlighting a linear relationship between total liquid displacement and applied strain percentage for mid- and high-curvature channels. In contrast, for low-curvature channels, the linear relationship is observed only within the 0–10% strain interval. Beyond this range, increasing strain does not significantly affect total liquid displacement. This behavior is attributed to the flattening of the shell at lower strain levels in low-curvature channels when tensile strain is applied, limiting further fluid displacement at higher strains.

To evaluate the pressure generation capabilities of different microchannel types when tensile strain is applied, we employed two different strategies and the results are shown in Fig. 3g. For the calculated maximum pressure measurement, we assumed that at 20% strain, the microchannel are fully flattened, resulting in a rectangular cross-section. Hagen–Poiseuille equation, which relates pressure difference to flow rate through the hydraulic resistance of the channel, is used to calculate maximum pressure (more information can be found in the SI material).

To calculate the maximum pressure using an experimental method, we utilized the setup shown in Fig. S5a. In this setup, an additional component—a sealed air reservoir—was incorporated as previously demonstrated to measure the liquid pressure in closed containers.[58] Since the pressure of an OSMiC does not remain constant under strain, we have measured the maximum pressure (see SI material for details). We have repeated the pressure measurement experiment with varying air reservoir volumes. We have observed that the smaller air reservoir volumes ($V_{\text{reservoir}} < 0.1$ μL) add a significant mechanical load influencing our measurement and reducing the maximum pressure (see Fig. S5b). Therefore, we have used $V_{\text{reservoir}}$ = 0.35 μL for measuring the maximum pressure and showed this as the measured data in Fig. 3g. In both the measured (orange) and calculated (gray) maximum forward pressures, it is evident that high-curvature channels generate significantly higher pressures compared to low-curvature channels.

Thus far, we have presented the results for low-, mid-, and high-curvature channels, specifically for a shell thickness of 50 μm. To expand our understanding, the maximum pressure is also calculated for various microchannel configurations with different shell thicknesses and corresponding Q values (Fig. 3h). Fig. 3h displays cross-section images of channels with varying curvature parameters (Q = 0.5, 1, 2, 4 with 80 μm shell thickness and Q = 5 with 50 μm shell thickness) (top) alongside corresponding maximum forward pressures ($P_{\text{max-forward}}$) for different shell thicknesses (30 μm, 50 μm, and 80 μm) across various Q values (bottom). The channels with Q = 0.5 exhibit a distinct behavior under tensile strain. When strain is applied, these channels push liquid slowly and with reduced displacement compared to devices with higher Q. Upon strain release, the displaced liquid does not retract. This behavior results from membrane sagging, which induces permanent channel deformation. The lack of sufficient curvature prevents the membrane from maintaining its structural integrity (Video S4), leading to this non-recoverable collapse without the characteristic snap-through behavior observed in channels with higher Q values. As Q increases, $P_{\text{max-forward}}$ shows a corresponding increase for the channels with 80 μm and 30 μm shell thickness. A similar trend is observed for increasing Q values at 50 μm shell thickness; however, at Q = 5, $P_{\text{max-forward}}$ decreases for the 50 μm shell thickness configuration. All channels with 80 μm shell thickness exhibit fully recoverable (snap-back) behavior (except Q = 0.5). The channels with a 30 μm shell thickness exhibit non-recoverable buckling (snap-through) at Q = 4 and 5. However, at higher curvatures (Q = 7), the channels display recoverable (snap-back) behavior. Overall, higher Q values and thicker shells produce greater maximum pressures, with the highest pressure (∼17 kPa) achieved at Q = 4 with 80 μm shell thickness.

The maximum pressure values during application/release of strain vary significantly based on shell thickness and Q (Fig. 3i). The channels with 30 μm shells at Q = 7 (snap-back) exhibit nearly symmetric forward and backward pressure. In contrast, 50 μm shells at Q = 4 (snap-back) show asymmetric pressure, with backward pressure exceeding forward pressure by nearly 30%. However, for 30 μm shells at Q = 4 (snap-through), backward pressure is eliminated because the shell remains permanently buckled after strain release, preventing fluid retraction.

The displaced liquid volume resulting from strain application (pushed liquid) at various strain levels (5%, 10%, 15%, and 20%) and Q values, along with their association with fabrication conditions, are presented in Fig. S6.

It is also observed that OSMiC structures respond selectively to the direction of applied strain, with significant liquid displacement occurring only when strain is applied in the *y*-direction (perpendicular to the channel). Uniaxial strain in the *x*-direction results in no liquid movement. Notably, biaxial strain (ε_x = 20%; ε_y = 20%) leads to enhanced liquid displacement compared to uniaxial conditions, as shown in Fig. S2b and c. The temporal response profiles presented in Fig. S2d further highlight the influence of boundary conditions on system dynamics, with free boundaries (*i.e.*, compression and wrinkling) yielding faster response times (τ = 1.4 s) compared to fixed (*i.e.*, no compression and no wrinkling) boundaries (τ = 2.1 s). Additionally, the linear relationship between applied strain percentage and liquid displacement across three distinct measurement locations (L1, L2, L3), each corresponding to progressively larger initial liquid volumes in the channel, is demonstrated in Fig. S2e. This relationship reveals that liquid displacement increases proportionally with both the applied strain percentage (ranging from 0% to 20%) and the initial liquid volume.

To further investigate and recreate the strain and vacuum loading effects on shell morphing under controlled conditions, additional control experiments were conducted. We tested three distinct conditions: vacuum integrated with strain, vacuum without strain, and strain without vacuum. In Fig. 4a, the top row shows the shell response to strain for microchannel corresponds to Q = 4 shown in Fig. 2: beginning with an initial undeformed state, then strain application (ε = 20%) generates visible shell wrinkling patterns, and finally strain release (ε = 0) induces periodic shell buckling due to vacuum generation within the channel. After a waiting period (5 s), the shell fully recovers its initial shape. The middle row illustrates the combined effect of strain and vacuum (−10 mbar), producing more pronounced

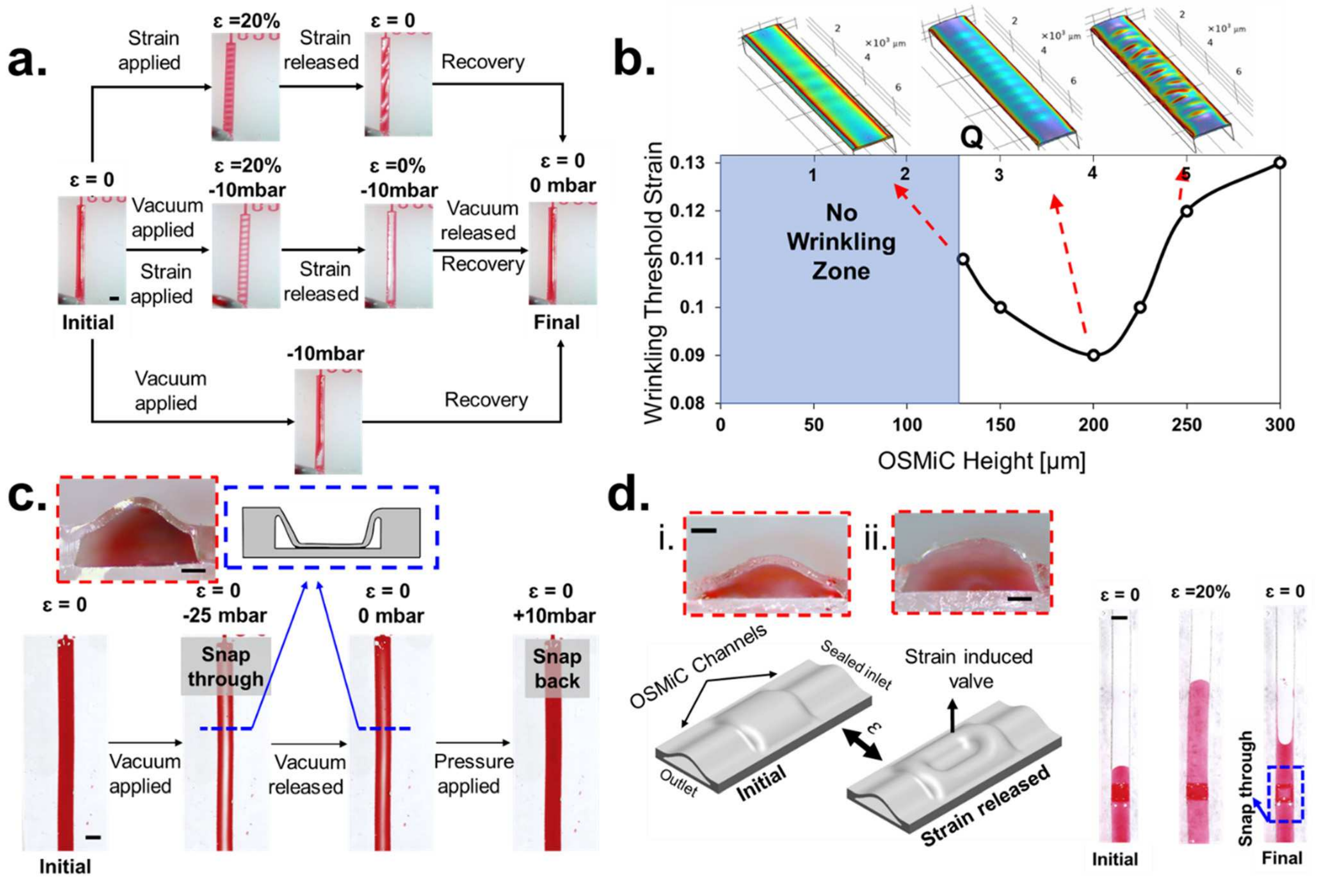

Fig. 4 The effect of loading (vacuum and strain) on various OSMiC structures. (a) Top-down photos of the microchannel (corresponds to Q = 4 shown in Fig. 2) under various loading and unloading configurations. The top row is the shell response during a strain-only cycle: beginning from an initial undeformed state to strain application (ε = 20%) to strain release (ε = 0). The middle row shows the combined effect of strain and vacuum (−10 mbar). The bottom row exhibits vacuum effects (−10 mbar) without strain. Scale bar: 1 mm. (b) Computational modeling of wrinkling threshold strain as a function of OSMiC channel height for channels with 50 μm shell thickness. The inset 3D simulation snapshots (top) illustrate representative deformation modes of OSMiC channels at different heights, corresponding to the data points in the plot. (c) Top-down photos of structure (h_{base} = 270 μm and h = 220 μm) under various vacuum conditions, illustrating morphing dynamics when additional room for shell deformation is provided. Scale bar: 1 mm. The inset image (red dashed boxes) provides a cross-section image of the microchannel. Scale bar: 200 μm. The inset image (blue dashed boxes) provides a schematic cross-section image of the snap-through microchannel. (d) (i) – Cross-sectional image of the microchannel with h_{base} = 80 μm, t_{m} = 80 μm, Q = 3. Scale bar: 200 μm. (ii) – Cross-sectional image of the microchannel with h_{base} = 230 μm, t_{m} = 30 μm, Q = 5. Schematic illustration of an integrated OSMiC system that combines the structures (left). Experimental validation of the strain-induced valve operation, showing the transition from the initial state to the final state (ε = 20%) (right). Scale bar: 1 mm.

and wider wrinkling patterns compared to the strain-only condition. Upon strain release, while maintaining vacuum, the shell exhibits complete buckling rather than the periodic buckling seen in the strain-only condition. Full recovery occurs after vacuum release, demonstrating reversible deformation. The bottom row exhibits vacuum effects (−10 mbar) without strain, resulting in only partial shell buckling —significantly less deformation than observed with combined strain-vacuum application. This comparison highlights how strain-induced wrinkles promote and enhance subsequent buckling by creating mechanical instabilities in the shell structure. The complete sequence demonstrates the channel's recovery to its original configuration after all testing conditions, indicating that the channel maintains its position in stable state 1 without transitioning to stable state 2 throughout the experimental process. The experimental results were compared to computational simulations. Consistent with the experimental observations, the simulations confirm that the synergistic application of vacuum and strain facilitates the formation of wrinkles and induces buckling behavior as shown in Fig. S7a.

Computational modeling provides further insight into the mechanical behavior of OSMiC channels by examining the relationship between OSMiC height and wrinkling threshold strain (Fig. 4b). At a fixed shell thickness of 50 μm, channels with reduced Q initially exhibit greater resistance to wrinkling, while their tendency to deform increases as the Q approaches 4. Beyond this critical point, taller channels demonstrate improved wrinkling resistance, revealing a non-monotonic behavior. The influence of Q on the wrinkling threshold strain is also explored for different shell thicknesses (t_m = 30 μm, t_m = 100 μm) in Fig. S7b. The results indicate that thicker shell require larger Q and higher strains to induce wrinkling.

To demonstrate that high-curvature channels can also transition from stable state 1 to stable state 2, when provided with additional space for shell deformation, we have tested the structure shown in Fig. 4c. Fig. 4c illustrates an experiment with only controlled vacuum application. This larger base height provides additional room for shell deformation, facilitating the snap-through behavior previously observed only in lower curvature channels. When a vacuum (−25 mbar) is applied, the shell buckles, transitioning into a deformed state. Unlike the microchannel in Fig. 4a, where the shell fully recovers after vacuum release, the shell here does not recover and instead remains in a buckled configuration, demonstrating snap-through behavior. This indicates bistable behavior, where the larger base height allows the shell to deform further and transition into a stable state 2. To restore the shell to its initial state (stable state 1), a positive pressure of +10 mbar is required.

Finally, an integrated system was developed to utilize the high-pressure generation capability while enabling controllable shell buckling. This integrated design combines a long section of Q = 3 (t_m = 80 μm), shown in Fig. 4d.i, and a square section with Q = 5 (t_m = 30 μm) in the center of the microchannel with 230 μm base height that functions as a strain-induced valve under tensile strain (shown in Fig. 4d.ii). Fig. 4d (left) presents a schematic illustration of this integrated OSMiC system. The design incorporates a sealed inlet, outlet, and strain-induced valve mechanism that regulates fluid movement between channel segments. Arrows indicate the direction of applied strain (ε) that activates the valve function. The strain-induced valve operates based on the difference in shell properties at the center of the device. The center section features a comparatively thinner shell and greater base height, providing more room for deformation. When tensile strain is applied, the OSMiCs (Q = 3, t_m = 80 μm) generate substantial pressure that pushes the liquid through the system. Under normal circumstances with uniform channel geometry, the liquid would fully return to its initial position upon strain release due to the snap-back behavior of high-curvature channels. However, in this integrated design, when strain is released, the center section with its thinner shell and increased base height undergoes buckling, effectively blocking the return flow path. This localized morphing prevents the liquid from fully returning to its initial position, thereby creating a one-way valve function that is activated solely by the application and release of strain. This mechanism demonstrates how geometric variations within a single integrated system can create a functional valve behavior without additional components or external control systems. Fig. 4d (right) shows the experimental validation of the strain-induced valve operation actuated with a 20% strain.

Following the benchtop characterization, the low-curvature and high-curvature channels (t_m = 50 μm) were tested on a volunteer human subject's wrist. Fig. 5 presents the wearable fluid control *via* snap-through morphing dynamics for potential drug delivery applications. Fig. 5a displays photographs of the microfluidic chip on a human subject's wrist, illustrating the distinct behaviors of low-curvature (top row) and high-curvature (bottom row) channels under different strain conditions: initial state (ε = 0), strained state (wrist extension), and after strain release (wrist relaxation). Consistent with benchtop experimental findings, when tensile strain is applied during wrist extension, the working liquid is pushed and transferred to the patch area in both channel types. Upon strain release (wrist relaxation), the two channel types exhibit noticeably different behaviors. In low-curvature channels, shell buckles, and the displaced liquid remain in the patch area, demonstrating the non-recoverable nature of these channels. In contrast, high-curvature channels exhibit complete fluid retraction after strain release, with the displaced liquid flowing back to its initial position due to the snap-back behavior of the shell. For high-curvature channels, the blue-outlined time-lapse sequence (t = 240 ms to t = 1 s after strain release) reveals rapid fluid displacement dynamics as the shell recovers its original shape, demonstrating snap-back behavior. SI videos illustrating liquid displacement on a human subject's wrist are provided for low-, and high-curvature channels in Videos S5 and S6, respectively.

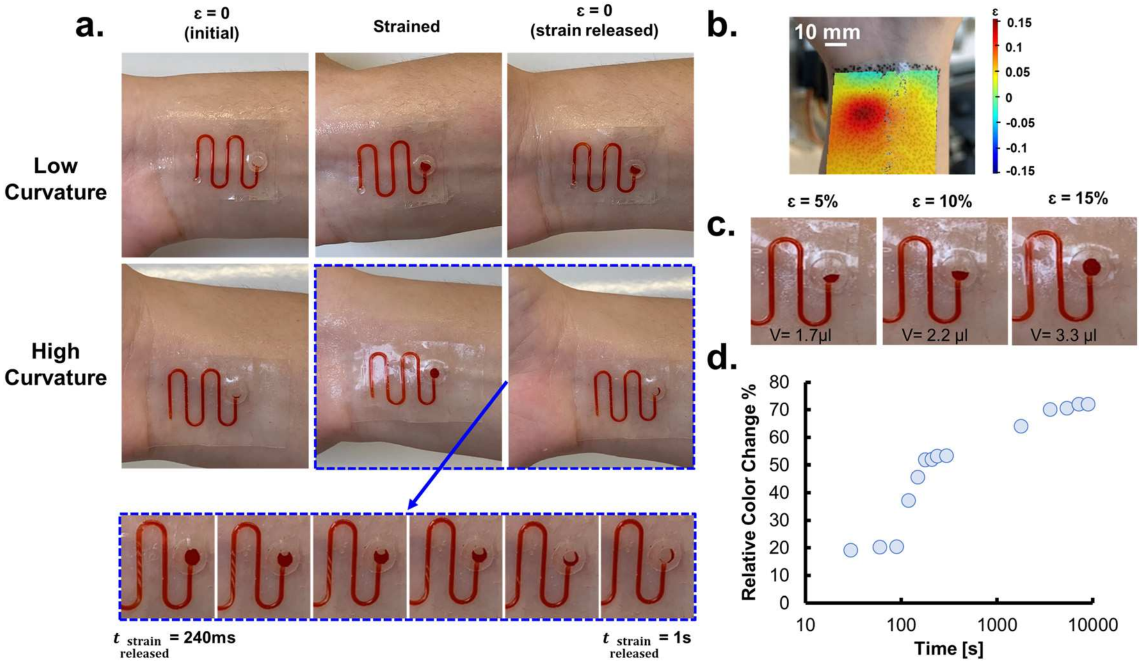

Fig. 5 Demonstration of wearable fluid control *via* snap-through morphing dynamics for drug delivery applications. (a) Photographs of the microfluidic chip on a human subject's wrist showing distinct behaviors of low-curvature (top row) and high-curvature (bottom row) channels under different strain conditions: initial state ($\varepsilon = 0$), strained state (wrist extension), and after strain release (wrist relaxation). For high-curvature channels, the blue-outlined time-lapse sequence (t = 240 ms to t = 1 s after strain release) reveals rapid fluid displacement dynamics as the shell recovers its original shape, demonstrating snap-back behavior. (b) Strain field heat maps (in the direction perpendicular to the OSMiC) during wrist extension, were obtained using digital image correlation (DIC) analysis. (c) Strain-dependent fluid displacement in high-curvature channels at increasing strain levels (5%, 10%, and 15%), with corresponding delivered volumes of 1.7 μL, 2.2 μL, and 3.3 μL, demonstrating linear volume-strain relationship. (d) Quantitative analysis of the colorimetric response over time was performed using a hydrocolloid patch integrated with a thin, flexible polymer layer.

To measure the skin strain field, 2D digital image correlation (DIC)[46] was utilized, as shown in Fig. 5b. Fig. 5c illustrates the fluid displacement in high-curvature channels at increasing maximum strain levels calculated using 2D DIC (5%, 10%, and 15%), corresponding to delivered volumes of 1.7 μL, 2.2 μL, and 3.3 μL, respectively, in reasonable agreement with the benchtop results shown in Fig. 3f. These results demonstrate a linear relationship between applied strain and delivered fluid volume, indicating control over dosage through mechanical deformations. Fig. 5d presents a quantitative analysis of the colorimetric response over time, especially relevant for irreversible $Q = 4$ scenario, showing relative color change percentage as an indicator of cumulative fluid delivery to the patch. The graph displays the long-term delivery profile (0–10 000 seconds) with *a* curve reaching approximately 75% saturation, while the initial delivery phase (0–360 seconds) highlights the early-stage colorimetric response dynamics.

Discussion

The OSMiCs with stiff shells behave linearly thus are only suitable to provide reversible fluid flow patterns with symmetrical pressures in forward and backward directions. However, as shells get thinner, which is also needed for conformal skin contact, the negative fluid pressure during the strain release phase of the movement cycle along with the shell wrinkling cause the shell to deviate from the linear behavior leading to morphing. The nonlinear deformation dynamics of the shell are responsible for the morphing. The morphing allows asymmetric flow, which is especially useful for obtaining functions such as fluid injection or suction (*i.e.*, pumping) using wearable microfluidic devices. For fluid pumping, maintaining consistent pressure values for a given input, independent of the output load is an important requirement. The morphing OSMiC shell relies on the low bending stiffness for achieving the nonlinearities required for pumping, which makes the device sensitive to the output load as also shown in Fig. S5b. Therefore, the Q value of the OSMiC shells should be chosen in accordance with the typical load expected in a given application. For the human subject experiments shown in Fig. 5, the patches, both $Q = 2$ and $Q = 4$, behaved very similarly to the benchtop experiments because we used a patch size that does not increase the output load significantly. This demonstrates that the skin is capable of providing the necessary input to administer a fluid on the skin when the output load is carefully adjusted. It can be argued that, for drug injection under the skin, the needle diameter or needle array size can be adjusted to have a similar control over the output load. The other alternative to achieve asymmetry is to use stiffer OSMiC shell integrated with discrete control elements shown in Fig. 4d.

To enable consistent fluid delivery during prolonged repetitive motion, such as throughout the day, integration of the microfluidic channel network with a refillable supply reservoir is essential to maintain fluid volume and sustain continuous operation over multiple cycles. A promising solution involves integrating the microfluidic channel network with a refillable supply reservoir, which can actively replenish the system and sustain continuous fluid transport over multiple cycles.

Furthermore, effective and predictable perfusion performance can be achieved through the use of digital image correlation (DIC) analysis prior to device placement. This technique enables precise mapping of strain distribution during typical body movements (*e.g.*, walking), allowing the device to be positioned on anatomical regions that exhibit favorable strain amplitudes. Such personalized placement ensures that a targeted fluid volume is delivered consistently and efficiently, aligning device performance with user-specific motion profiles.

To address application-specific performance needs, we outline the design logic for selecting and tuning the two key structural parameters—shell thickness and the Q. For practical device design, a two-step approach is recommended. First, the shell thickness should be selected based on application-specific constraints, such as material limits, fabrication considerations, or required input pressure. Once thickness is fixed, the Q value can be tuned by adjusting the dome geometry to optimize the desired dynamic response. This sequential design logic provides a straightforward and adaptable framework for tailoring the mechanical behavior of the OSMiC shell to meet various operational demands.

The soft-lithography technique we have developed enables the fabrication of OSMiC patches reproducibly. Even though we have not analyzed the limits of the technique fully and focused on the interactions between the morphing and fluid flow here, we were able to fabricate OSMiC patches as thin as 200 μm with a Q value as high as 7. Another factor in the functionality of OSMiC patches is the channel width. We have created OSMiCs with a width as narrow as 300 μm, which exhibit Q values larger than 6. However, to focus on the effect of Q on the device performance we have not included these results here.

During our investigation, channel base height emerged as an unexpected pivotal factor for enabling the snap-back behavior. Even when the vacuum load on the shell is sufficient to induce a snap-through movement, the base channel does not allow the shell to reach a stable state; hence cause a snap-back. This observation highlights the interplay between geometric constraints and bistability, offering an additional design parameter for fine-tuning the mechanical response of OSMiC structures to meet specific application requirements.

Computational modeling further explains the relationship between OSMiC height and wrinkling threshold strain. For a fixed shell thickness of 50 μm, channels with reduced OSMiC heights initially exhibit greater resistance to wrinkling. However, as OSMiC height approaches 200 μm, wrinkling tendency increases. Beyond this critical point, taller channels demonstrate higher wrinkling resistance. This is explained by the additional wrinkling modes allowed in higher Q channels, as observed by the irregular wrinkling pattern for the channel with 250 μm height (Q = 5) in Fig. 4b inset compared to others. This computational finding aligns with experimental observations (Fig. 3h), where OSMiC structures with Q = 4 generate greater maximum pressure than those with Q = 5 for a shell thickness of 50 μm. This correlation suggests a potential relationship between wrinkling behavior and pressure performance in OSMiC systems. While further investigation is needed to fully understand this connection, our findings emphasize the importance of optimizing channel dimensions to balance mechanical deformations and functional performance.

Conclusion

In this study, we address a key limitation in power-free wearable microfluidic devices—the lack of fluidic pumping and control (*e.g.*, valve)—by developing an out-of-surface microchannel (OSMiC) structure and its fabrication method. The OSMiC design features an arched shell that generates positive pressure under tensile strain, which actively propels a working liquid toward an outlet. By controlling the architecture of the shell, we obtained nonlinear deformation characteristics that led to self-morphing (*i.e.*, channel shape-change that occurs during strain release phase). We showed that thin shells, which are particularly suitable for wearable devices due to their superior conformality and flexibility, display either snap-through or snap-back behavior depending on their aspect ratios (*i.e.*, Q). Our results highlighted that higher curvature is essential for achieving snap-back behavior, albeit there is an additional factor of wrinkling that needs to be considered for optimizing the geometry for maximum pressure generation using thin shells.

The effects of strain and vacuum on morphing dynamics were investigated experimentally and through numerical simulations. An integrated system that leverages the high-pressure (10 kPa) generation capabilities of OSMiC structures while incorporating controllable shell morphing mechanisms, functioning as a strain-induced valve activated by tensile strain, was developed to be used for more efficient fluid pumping as a future goal. Finally, we successfully integrated OSMiCs into a skin-mountable patch demonstrating its suitability for wearable drug delivery in human subject tests. Looking forward, this platform may be extended to include microneedle arrays for controlled transdermal administration. In such a configuration, the OSMiC shell can serve as a mechanically actuated pumping unit to drive precise volumes of fluid through hollow or porous microneedles, enabling controlled transdermal delivery. By tuning the shell geometry (*e.g.*, Q and shell thickness), the pressure output can be matched to the resistance of the microneedle array, ensuring reliable dosing without the need for external power. The findings from this study will open up possibilities in wide range of fields such as soft robotics, adaptive prosthetics, point-of-care diagnostics, and drug delivery.

Ethics statement

All experiments were performed in accordance with the institutional guidelines and approved by the Institutional Review Board at Santa Clara University with protocol number 21-06-1630. Informed consent was obtained from the human participant.

Author contributions

I. E. A. and R. A. designed the research and wrote the manuscript; R. A. performed the experiments and analyzed the data; R. A. and J. B. fabricated the chips; H. G. performed 2D DIC analysis; H. G. and M. M. B. fabricated the chips using photolithography molds; I. E. A. and K. O. performed the computational modeling; I. E. A. guided the whole research. All authors have read and agreed to the published version of the manuscript.

Conflicts of interest

The authors declare no competing financial or non-financial interests.

Data availability

Supplementary information is available, providing details of pressure calculations, fabrication characterization, strain-dependent liquid displacement analyses, cyclic actuation data, maximum pressure measurements, and computational modeling results, together with supporting Fig. S1–S7. See DOI: **https://doi.org/10.1039/D5LC00417A**.

Some data supporting this article are provided as supplementary materials, including images and videos. The remaining data can be found at the following link: **https://drive.google.com/drive/folders/190x5QK82IusKFpSPS6EXx1gZZ6-lsdpF?usp=drive_link**.

Acknowledgements

This project was supported by the NSF program 19-582, grant 2045087. The device was fabricated in the Center for Nanostructures at Santa Clara University.

References

1 X. Yang, *et al.*, Flexible, wearable microfluidic contact lens with capillary networks for tear diagnostics, *J. Mater. Sci.*, 2020, **55**, 9551–9561.
2 K. M. Clark and T. R. Ray, Recent Advances in Skin-Interfaced Wearable Sweat Sensors: Opportunities for Equitable Personalized Medicine and Global Health Diagnostics, *ACS Sens.*, 2023, **8**(10), 3606–3622, DOI: **10.1021/ACSSENSORS.3C01512**.
3 J. Xu, *et al.*, Wearable Biosensors for Non-Invasive Sweat Diagnostics, *Biosensors*, 2021, **11**, 245.
4 T. Lehnert and M. A. M. Gijs, Microfluidic systems for infectious disease diagnostics, *Lab Chip*, 2024, **24**, 1441–1493.
5 S. Cheng, *et al.*, Recent Progress in Intelligent Wearable Sensors for Health Monitoring and Wound Healing Based on Biofluids, *Front. Bioeng. Biotechnol.*, 2021, **9**, 765987.
6 Y. Xiang, *et al.*, Battery-Free and Multifunctional Microfluidic Janus Wound Dressing with Biofluid Management, Multi-Indicator Monitoring, and Antibacterial Properties, *ACS Appl. Mater. Interfaces*, 2024, **16**, 50321–50334.
7 M. Mohammadi, *et al.*, Navigating the future: Microfluidics charting new routes in drug delivery, *Int. J. Pharm.*, 2024, 124142, DOI: **10.1016/J.IJPHARM.2024.124142**.
8 M. Padash, C. Enz and S. Carrara, Microfluidics by Additive Manufacturing for Wearable Biosensors: A Review, *Sensors*, 2020, **20**(15), 4236, DOI: **10.3390/s20154236**.
9 B. Khadka, B. Lee and K. T. Kim, Drug Delivery Systems for Personal Healthcare by Smart Wearable Patch System, *Biomolecules*, 2023, **13**(6), 929, DOI: **10.3390/biom13060929**.
10 K. Guk, *et al.*, Evolution of Wearable Devices with Real-Time Disease Monitoring for Personalized Healthcare, *Nanomaterials*, 2019, **9**, 813.
11 G. Chen, X. Liu, S. Li, M. Dong and D. Jiang, A droplet energy harvesting and actuation system for self-powered digital microfluidics, *Lab Chip*, 2018, **18**, 1026–1034.
12 Z. H. Guo, *et al.*, Self-Powered Electrowetting Valve for Instantaneous and Simultaneous Actuation of Paper-Based Microfluidic Assays, *Adv. Funct. Mater.*, 2019, **29**, 1808974.
13 S. Zhao, *et al.*, A wearable osmotic microneedle patch provides high-capacity sustained drug delivery in animal models, *Sci. Transl. Med.*, 2024, **16**(775), eadp3611, DOI: **10.1126/scitranslmed.adp3611**.
14 Y. Zhang, J. Yu, Y. Zhu and Z. Gu, Elastic drug delivery: Could treatments be triggered by patient movement?, *Nanomedicine*, 2016, **11**(4), 323–325, DOI: **10.2217/nnm.15.197**.
15 S. E. Alavi, *et al.*, Microfluidics for personalized drug delivery, *Drug Discovery Today*, 2024, **29**, 103936.
16 J. Wang, J. A. Kaplan, Y. L. Colson and M. W. Grinstaff, Stretch-Induced Drug Delivery from Superhydrophobic Polymer Composites: Use of Crack Propagation Failure Modes for Controlling Release Rates, *Angew. Chem.*, 2016, **128**, 2846–2850.
17 J. Manikkath and J. A. Subramony, Toward closed-loop drug delivery: Integrating wearable technologies with transdermal drug delivery systems, *Adv. Drug Delivery Rev.*, 2021, **179**, 113997, DOI: **10.1016/j.addr.2021.113997**.
18 Y. Liu, L. Yang and Y. Cui, A wearable, rapidly manufacturable, stability-enhancing microneedle patch for closed-loop diabetes management, *Microsyst. Nanoeng.*, 2024, **10**, 1–15.

19 Z. Zheng, R. Zhu, I. Peng, Z. Xu and Y. Jiang, Wearable and implantable biosensors: mechanisms and applications in closed-loop therapeutic systems, *J. Mater. Chem. B*, 2024, **12**, 8577.

20 C. Yang, *et al.*, Intelligent wireless theranostic contact lens for electrical sensing and regulation of intraocular pressure, *Nat. Commun.*, 2022, **13**, 1–15.

21 H. Joo, *et al.*, Soft implantable drug delivery device integrated wirelessly with wearable devices to treat fatal seizures, *Sci. Adv.*, 2021, **7**(1), eabd4639, DOI: **10.1126/sciadv.abd4639**.

22 C. B. Askar, N. Cmager, R. Altay and I. E. Araci, Human Activity Recording Based on Skin-Strain-Actuated Microfluidic Pumping in Asymmetrically Designed Micro-Channels, *Sensors*, 2024, **24**(13), 4207, DOI: **10.3390/s24134207**.

23 Y. Liu, *et al.*, Strain-Tunable Microfluidic Devices with Crack and Wrinkle Microvalves for Microsphere Screening and Fluidic Logic Gates, *ACS Appl. Mater. Interfaces*, 2021, **13**, 36849–36858.

24 H. Fallahi, *et al.*, On-demand deterministic release of particles and cells using stretchable microfluidics, *Nanoscale Horiz.*, 2022, **7**, 414–424.

25 J. Park and J. K. Park, Integrated microfluidic pumps and valves operated by finger actuation, *Lab Chip*, 2019, **19**, 2973–2977.

26 K. Iwai, *et al.*, Finger-powered microfluidic systems using multilayer soft lithography and injection molding processes, *Lab Chip*, 2014, **14**, 3790–3799.

27 X. Le, *et al.*, A Finger-Actuated Sample-Dosing Capillary-Driven Microfluidic Device for Loop-Mediated Isothermal Amplification, *Biosensors*, 2024, **14**, 410.

28 J. T. Reeder, *et al.*, Resettable skin interfaced microfluidic sweat collection devices with chemesthetic hydration feedback, *Nat. Commun.*, 2019, **10**(1), 5513, DOI: **10.1038/s41467-019-13431-8**.

29 J. Di, *et al.*, Stretch-Triggered Drug Delivery from Wearable Elastomer Films Containing Therapeutic Depots, *ACS Nano*, 2015, **9**, 9407–9415.

30 A. Brinkmeyer, M. Santer, A. Pirrera and P. M. Weaver, Pseudo-bistable self-actuated domes for morphing applications, *Int. J. Solids Struct.*, 2012, **49**, 1077–1087.

31 M. Gomez, D. E. Moulton and D. Vella, Passive Control of Viscous Flow via Elastic Snap-Through, *Phys. Rev. Lett.*, 2017, **119**, 144502, DOI: **10.1103/PhysRevLett.119.144502**.

32 O. Oshri, K. Goncharuk and Y. Feldman, Snap-induced flow in a closed channel, *J. Fluid Mech.*, 2024, **986**, A12, DOI: **10.1017/jfm.2024.312**.

33 H. Kim, M. Lahooti, J. Kim and D. Kim, Flow-induced periodic snap-through dynamics, *J. Fluid Mech.*, 2021, **913**, A52.

34 X. Zhang, A. E. Oseyemi, K. Ma and S. Yu, Entirely soft valve leveraging snap-through instability for passive flow control, *Sens. Actuators, B*, 2022, **367**(15), 132035, DOI: **10.1016/j.snb.2022.132035**.

35 D. P. Holmes, B. Tavakol, G. Froehlicher and H. A. Stone, Control and manipulation of microfluidic flow via elastic deformations, *Soft Matter*, 2013, **9**, 7049–7053.

36 J. Kang, C. Wang, Z. Xue, M. Liu and H. Tan, Buckling delamination induced microchannel: Flow regulation in microfluidic devices, *Appl. Phys. Lett.*, 2016, **109**(10), 103503, DOI: **10.1063/1.4962429**.

37 D. P. Holmes, Elasticity and stability of shape-shifting structures, *Curr. Opin. Colloid Interface Sci.*, 2019, **40**, 118–137.

38 Y. Chi, *et al.*, Bistable and Multistable Actuators for Soft Robots: Structures, Materials, and Functionalities, *Adv. Mater.*, 2022, **34**(19), 2110384, DOI: **10.1002/adma.202110384**.

39 Y. Forterre, J. M. Skotheim, J. Dumals and L. Mahadevan, How the Venus flytrap snaps, *Nature*, 2005, **433**, 421–425.

40 R. Sachse, *et al.*, Snapping mechanics of the Venus flytrap (Dionaea muscipula), *Proc. Natl. Acad. Sci. U. S. A.*, 2020, **117**, 16035–16042.

41 M. L. Smith, G. M. Yanega and A. Ruina, Elastic instability model of rapid beak closure in hummingbirds, *J. Theor. Biol.*, 2011, **282**, 41–51.

42 D. K. Patel, *et al.*, Highly Dynamic Bistable Soft Actuator for Reconfigurable Multimodal Soft Robots, *Adv. Mater. Technol.*, 2023, **8**, 2201259.

43 X. Zhang, *et al.*, A bioinspired snap-through metastructure for manipulating micro-objects, *Sci. Adv.*, 2022, **8**(46), eadd4768, DOI: **10.1126/sciadv.add4768**.

44 P. B. Gonçalves, *et al.*, Dynamic non-linear behavior and stability of a ventricular assist device, *Int. J. Solids Struct.*, 2003, **40**, 5017–5035.

45 A. Kalnins, On Vibrations of Shallow Spherical Shells, *J. Acoust. Soc. Am.*, 1961, **33**, 1102–1107.

46 H. Gasvoda, N. Cmager, R. Altay, J. Y. Lee and I. E. Araci, Integration of capillaric strain sensors toward recognition of human movements, *Sens. Diagn.*, 2023, **2**, 212–224.

47 H. Gasvoda, *et al.*, Computer-Aided Design of Integrated Digital Strain Sensors for Hardware-Based Recognition and Quantification of Human Movements, *Adv. Sens. Res.*, 2025, **4**(4), 2400146, DOI: **10.1002/adsr.202400146**.

48 S. Agaoglu, *et al.*, Ultra-sensitive microfluidic wearable strain sensor for intraocular pressure monitoring, *Lab Chip*, 2018, **18**, 3471–3483.

49 L. R. Yepes, *et al.*, Skin Mountable Capillaric Strain Sensor with Ultrahigh Sensitivity and Direction Specificity, *Adv. Mater. Technol.*, 2020, **5**(12), 2000631, DOI: **10.1002/admt.202000631**.

50 M. Farshad, *Design and Analysis of Shell Structures*, 1992, vol. 16.

51 I. E. Araci, *et al.*, Flow stabilization in wearable microfluidic sensors enables noise suppression, *Lab Chip*, 2019, **19**, 3899–3908.

52 S. W. Lee and S. S. Lee, Shrinkage ratio of PDMS and its alignment method for the wafer level process, *Microsyst. Technol.*, 2008, **14**, 205–208.

53 M. H. Madsen, N. A. Feidenhans'l, P.-E. Hansen, J. Garnæs and K. Dirscherl, Accounting for PDMS shrinkage when

replicating structures, *J. Micromech. Microeng.*, 2014, **24**, 127002.

54 V. Nayyar, K. Ravi-Chandar and R. Huang, Stretch-induced stress patterns and wrinkles in hyperelastic thin sheets, *Int. J. Solids Struct.*, 2011, **48**, 3471–3483.

55 T. Wang, Y. Yang and F. Xu, Mechanics of tension-induced film wrinkling and restabilization: A review, *Proc. R. Soc. A*, 2022, **478**(2263), 20220149, DOI: **10.1098/rspa.2022.0149**.

56 B. Li, F. Jia, Y. P. Cao, X. Q. Feng and H. Gao, Surface wrinkling patterns on a core-shell soft sphere, *Phys. Rev. Lett.*, 2011, **106**, 234301.

57 Y. P. Cao, B. Li and X. Q. Feng, Surface wrinkling and folding of core–shell soft cylinders, *Soft Matter*, 2011, **8**, 556–562.

58 I. E. Araci, B. Su, S. R. Quake and Y. Mandel, An implantable microfluidic device for self-monitoring of intraocular pressure, *Nat. Med.*, 2014, **20**, 1074–1078.